Controlling Dissolution of PbTe Nanoparticles in Organic Solvents during Liquid Cell Transmission Electron Microscopy

Journal:	*Nanoscale*
Manuscript ID	NR-COM-05-2019-004646
Article Type:	Communication
Date Submitted by the Author:	31-May-2019
Complete List of Authors:	Bhattarai, Nabraj; Naval Research Laboratory, NRC Postdoctoral Associate Woodall, Danielle; Naval Research Laboratory, NRC Postdoctoral Associate Boercker, Janice; Naval Research Laboratory, Electronics Science and Technology Division Tischler, Joseph; Naval Research Laboratory, Brintlinger, Todd; Naval Research Laboratory, Materials Science and Technology Division

SCHOLARONE™
Manuscripts

Controlling Dissolution of PbTe Nanoparticles in Organic Solvents during Liquid Cell Transmission Electron Microscopy

Nabraj Bhattarai,[1,2] Danielle L. Woodall,[1,2] Janice E. Boercker,[2] Joseph G. Tischler,[2] and Todd H. Brintlinger[2]

1. NRC Postdoctoral Associate, U.S. Naval Research Laboratory, Washington, DC, USA
2. U.S. Naval Research Laboratory, Washington, DC, USA

ABSTRACT

We present direct visualization of the dynamics of oleic-acid-capped PbTe nanoparticles suspended in different organic solvents using liquid cell transmission electron microscopy. Liquid cell transmission electron microscopy is a powerful tool to directly observe the behavior of a variety of nanoparticles in liquids, but requires careful consideration and quantification of how the electron beam affects the systems being investigated. We find that etching and dissolution of PbTe nanoparticles occurs with a strong dependence on electron dose rate ranging from no perceivable effect on the nanoparticles with lower dose rates (50 $e^-/Å^2/s$) to complete dissolution within seconds or minutes at higher dose rates (100 and 200 $e^-/Å^2/s$). We propose that oxidative etching, resulting from the radiolysis of small amounts of water, causes the PbTe nanoparticles to dissolve after exposure to a threshold electron dose rate of 50 $e^-/Å^2/s$.

1. INTRODUCTION

Due to their small bandgaps and efficient multi-exciton generation --among other useful properties-- together with a solution-based synthesis, lead chalcogen nanoparticles hold promise for improved performance in several different technologies, including solar cells[1], infrared detectors[2], and thermoelectrics[3]. These same properties are heavily dependent on nanoparticle size and morphology. In particular, PbTe nanorods may theoretically improve device performance over spherical PbTe nanoparticles, or PbSe or PbS nanorods, due to enhanced multi-exciton generation[4], enhanced absorption coefficient[5] and reduced Auger coefficients[6]. However, the synthesis of high quality, uniform PbTe nanorods with tunable diameters and lengths remains in its infancy compared to the synthesis of PbSe nanorods.[7-11]

The oriented attachment of component nanoparticles into high-aspect-ratio nanorods is one possible mechanism to synthesize PbTe nanorods. To probe this behavior, we used liquid cell transmission electron microscopy (LCTEM) to understand PbTe nanostructure formation.[12] LCTEM is a powerful tool which provides visual confirmation of dynamic processes present in their native synthesis environment,[13, 14] including oriented attachment,[15] faceted growth,[15] aggregation,[16] dissolution,[17, 18] formation of core-shell structures,[19] self-assembly,[20-22] and growth of nanoparticles with different morphologies.[23]

Even with the promise of this technique, LCTEM of nanoparticle colloids in liquids has challenges.[14, 24-26] The interaction of high-energy electrons with solvents produces numerous species of ions, radicals, charged compounds, and other metastable species with different lifetimes and reactivities[27, 28] which in turn alter the local chemistry. For example, the radiolysis of water produces charged species, e.g. ions, solvated electrons, and other radicals,[29] while the radiolysis of organic solvents (e.g. toluene) produces molecular hydrogen, bibenzyl radicals, and longer chain hydrocarbons.[30] While recent LCTEM studies have investigated the growth and dissolution of metal nanoparticles in non-aqueous media, including oriented attachment of metal nanoparticles into nanorods[15, 31, 32] and dissolution of metal nanoparticles in aqueous media as a result of beam-driven chemistry[17, 18, 33], LCTEM of semiconducting nanoparticles in non-aqueous solvents is fairly nascent. To this end, we present here the study of semiconductor (PbTe) nanoparticles in organic solvents using LCTEM of extant nanoparticles and evaluate the effect of electron irradiation at different dose rates. Specifically, we perform LCTEM experiments on oleic-acid-capped PbTe nanoparticles suspended in different organic solvents, either toluene or a mixture of dichlorobenzene (DCB) and pentadecene, and image them at high, medium, and low electron dose rates where complete, intermediate, and no dissolution of PbTe nanoparticles are observed, respectively.

2. EXPERIMENTAL

General Considerations: Unless otherwise noted, standard Schlenk-line techniques were used. Trioctylphosphine (90%), lead oxide (99.999%), tellurium shot (99.999%), oleic acid (90%), 1-octadecene (90%), *o*-dichlorobenzene (anhydrous 99%), pentadecane (≥99%), and anhydrous toluene and acetonitrile were purchased from Sigma Aldrich. All chemicals were used as received.

Synthesis: PbTe nanoparticles were synthesized using standard air-free techniques following the procedure from Murphy et al.[4] A 0.5 M trioctylphosphine telluride stock solution was prepared by dissolving tellurium shot in trioctylphosphine and stirring overnight in a glovebox. In a typical reaction, 0.225 g lead oxide, 1.89 g oleic acid, and 4.7 g of 1-octadecene were loaded into a three-neck flask. The solution was heated to 110 °C under vacuum for approximately one hour, and the solution turned from a cloudy red/yellow color to clear and colorless, indicating the formation of lead oleate. The flask was backfilled with argon, and the temperature was raised to 150 °C. Once the temperature stabilized, 1 mL of the 0.5 M trioctylphosphine telluride stock solution was rapidly injected, and the flask was immediately transferred to an oil bath heated to 115 °C. After 6 minutes, 2 mL of anhydrous toluene was injected into the flask followed by a transfer to an ice bath. All work up procedures were completed in a glovebox using anhydrous solvents. The synthesized PbTe nanoparticles were extracted from the growth solution by adding toluene and acetonitrile and centrifuging at 6000 rpm for 5 minutes. The supernatant was discarded, and the nanoparticles were washed a second time using the same procedure. Once the PbTe nanoparticles were purified, they were dried overnight, and then redispersed in either toluene or a mixture (1:1 by volume) of *o*-dichlorobenzene and pentadecene for TEM characterization. One sample was redispersed in water saturated toluene for LCTEM characterization. This water saturated toluene was created by mixing toluene with water such that two phases formed. This mixture was stirred for 20 mins before centrifuging at 6000 rpm for 5 minutes to create a sharp interface between to the two phases. Then the toluene phase was carefully pipetted off the water phase as to only collect the toluene. The concentration of water in this toluene is likely close to the solubility of water in toluene which is 0.027 M.[34]

Ex situ **Characterization**

i. **Scanning transmission electron microscopy using high-angle annular dark field (STEM-HAADF).** Following synthesis, PbTe nanoparticles were dispersed in toluene and drop-cast onto either lacey-carbon or graphene-enhanced lacey-carbon copper grids. For the ultra-high-vacuum imaging in our aberration-corrected STEM (Nion UltraSTEM200X), we first bake at 140 °C in vacuum before insertion into column.

ii. **High-resolution transmission electron microscopy (HRTEM).** As with STEM-HAADF preparation, nanoparticles were drop-cast onto lacey-carbon grids, and then inserted directly into the TEM (JEOL JEM-2200FS). No bake is required when using this TEM.

***In situ* Characterization - Liquid Cell Transmission Electron Microscopy**

i. **Fluid cell assembly.** The in situ LCTEM experiment was carried out using a commercial electrochemical single-port liquid cell system (Protochips Inc, Poseidon P500). Two commercially-provided silicon nitride membrane chips (Protochips EPB-42A1 and EPT-55W) were initially stripped of their protective photoresist using acetone and isopropanol. The chips and the tip of the holder were then plasma-cleaned using a combination Ar/O_3 plasma at 45 W for three minutes. Immediately following the plasma cleaning, the PbTe nanoparticles were deposited onto the larger silicon nitride membrane chip by drop casting a 0.5 μL solution of nanoparticles onto the chip. The smaller chip, with 10 x 10 μm^2 regions thinned to <20 nm silicon nitride thickness, was then inverted on top of the larger, mating chip and clamped inside the holder with metal retaining pieces and Viton O-rings. This drop-casting and cell assembly was done in air and represents the single longest exposure (1-5 min) of the nanoparticles to ambient conditions. The assembled LCTEM holder was tested for vacuum leaks on an external pumping station and then inserted into the TEM (JEOL JEM2200FS). Following 30 min in the column vacuum, the holder was exposed to the electron beam and imaging was started. In the first experiments, PbTe nanoparticles were dispersed from toluene, in the second experiment a mixture of dichlorobenzene and pentadecene (1:1 by volume) was used as the solvent, and in the third experiment toluene saturated with and water as described above.

ii. **In situ imaging using TEM.** Prior to insertion of the LCTEM holder, the TEM alignments were performed at 200 kV using a conventional holder and an alignment sample since LCTEM holders lack the conventional features for alignment procedures. During this 'pre-alignment', the condenser lens currents (JEOL CL3 value) were registered using external TEM control software (System in Frontier Inc. JEMtoolbox) and micrographs of the unobscured beam were acquired to correlate electron dose rates with lens currents. Accordingly, the condenser lens current was registered for each imaging dataset such that the corresponding electron dose rate can be calculated from the pre-acquired registry. All images were acquired using a high-speed electron camera (Gatan OneView) which allowed for multiple full-resolution frames per second.

iii. **Calculation of electron dose rates.** We utilized the parallel beam LCTEM where the beam is spread with irradiation on larger areas, allowing near steady state conditions. The electron dose rate was calculated from the previously-acquired registry of micrographs of the unobscured beam and re-verified after the *in situ* experiments were completed. For these calculations, we used the vendor-provided camera calibration of 40 counts/electron and divided by the screen size and acquisition time, e.g. for 6.79 x 10^7 total counts on an area of 258 x 258 nm^2 and acquisition time of 20 ms we arrive at 8.6 x10^3 $e^-/nm^2/s$.

3. RESULTS AND DISCUSSIONS

Before performing LCTEM, we characterized our nanoparticles with conventional *ex situ* TEM, and electron micrographs of our PbTe nanoparticles are presented in Fig. 1. The high-resolution transmission electron microscope (HRTEM) image in Fig. 1a shows a monodisperse collection of nanoparticles with diameters of 7.0 ± 0.4 nm and separations of 4 ± 0.4 nm between nanoparticle edges. The higher magnification HRTEM image in Fig. 1b indicates that individual nanoparticles are cuboctahedral with (200) and (220) terminated facets and with the characteristic lattice spacing for altaite, the mineral name for PbTe, which allows nanoparticle to be modeled as cuboctahedral as seen in Fig. 1c.[35, 36] We also performed energy dispersive spectroscopy (EDS) to confirm the chemical composition of the PbTe NPs (Fig. S1).

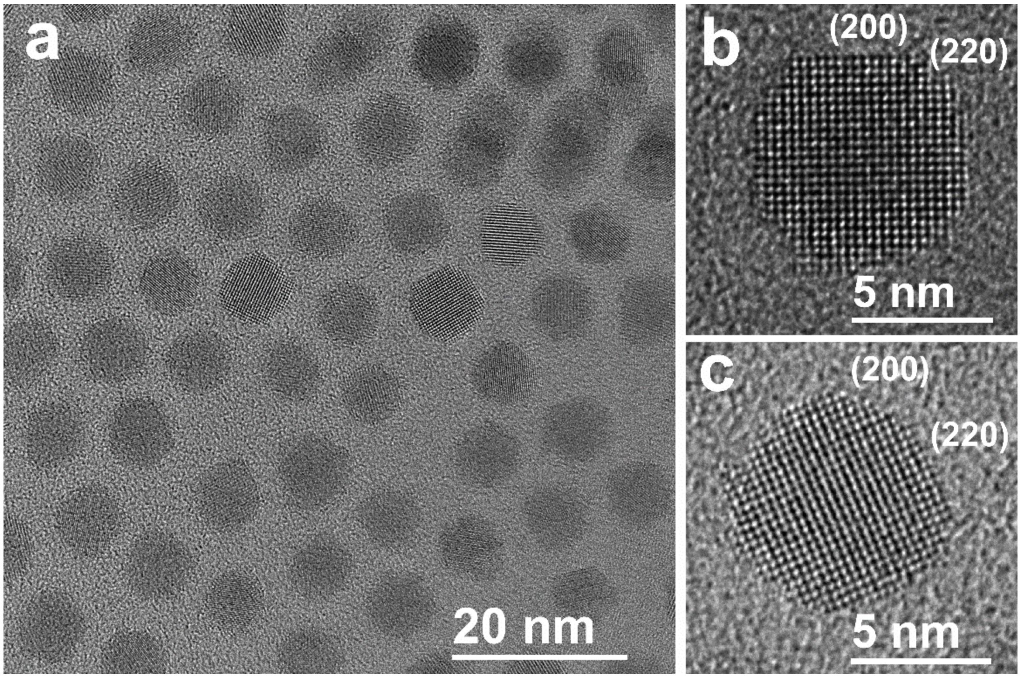

Figure 1. Electron micrographs of PbTe nanoparticles acquired *ex situ* a) TEM bright field micrograph of PbTe nanoparticles showing uniformity in size and morphology, where diameter is ~7.0 ± 0.4 nm and the morphology is cuboctahedral. b) HRTEM image of individual PbTe nanoparticle showing the crystal facets exposed as (200) and (220). c) Additional HRTEM of PbTe nanoparticles showing cuboctahdreal shape.

Having confirmed a uniform size distribution in our initial nanoparticles ensembles, we then performed LCTEM experiments as described in the Experimental section. We began with our highest electron dose rate (or fluence) of 200 $e^{-}/Å^{2}/s$ with nanoparticles in toluene, and individual frames of *in situ* video obtained for LCTEM are presented in Fig. 2 (taken from Video 1, SI). Following *ex situ* characterization, nanoparticles are presumed single crystal with cuboctahedron morphology; however, facets are not easily distinguishable *in situ* due to additional background scattering in both the membranes and the liquid. At t=1 s, the nanoparticles are well dispersed with the same size and spacing distributions as seen with *ex situ* TEM, 7.0 ± 0.4 nm diameters and 4 ± 0.4 nm separations. As time passes, adjacent particles aggregate and fuse as seen in frames at 60, 121, and 181 s, forming rod-like structures. After 241 seconds, some adjacent nanoparticles form multi-nanoparticle chains through random coalescence while other nanoparticles show evidence of etching, which is seen more distinctly in frames at 301 and 361 s. All the particles are completely dissolved after 421 s, as seen in the last frame of Fig. 2. For more details, see video 1 in SI.

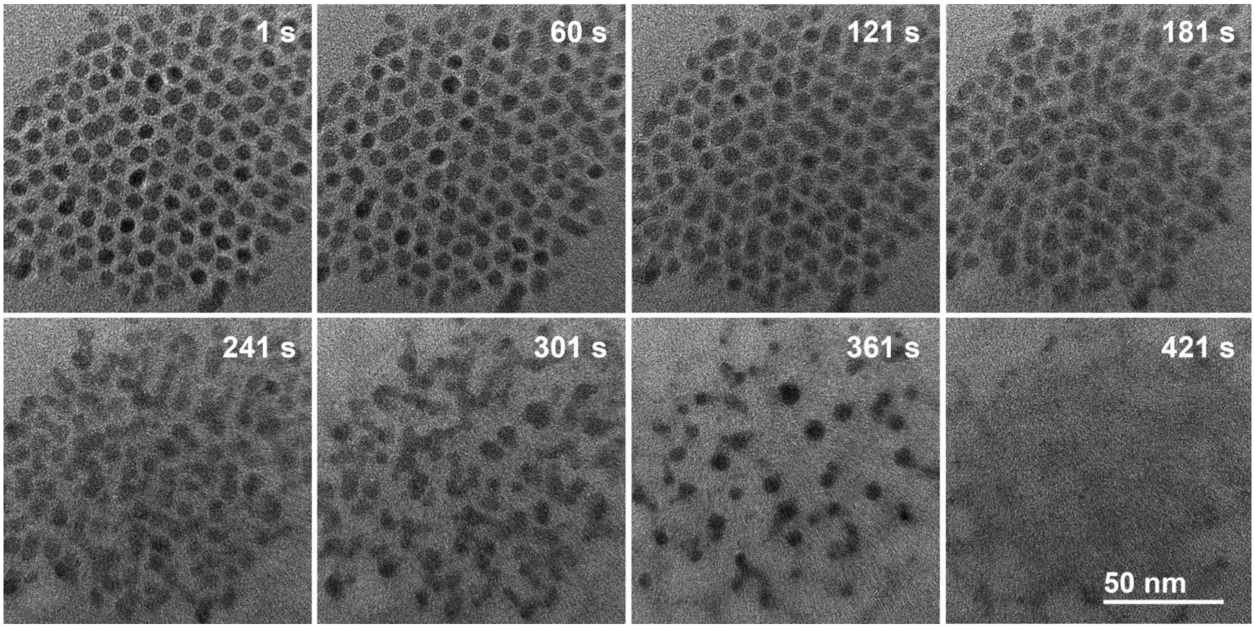

Figure 2. Bright field TEM images of dissolution of PbTe nanoparticles in toluene with an electron dose rate of 200 $e^-/Å^2/s$ (high dose rate) during LCTEM. The total elapsed time of exposure to the beam is shown on each frame.

We then exposed the nanoparticles in a nearby unirradiated region to a 'medium' electron dose rate (or fluence) of 100 $e^-/Å^2/s$ with individual frames shown in Fig. 3 (taken from Video 2, SI). As with the higher dose rate (Fig. 2) adjacent nanoparticles aggregate and fuse. However, this occurs over a larger length of time than with the higher dose rate, as seen in frames at 60, 121, 200 and 300 s in Fig. 3. After 300 s of exposure to the beam, some adjacent nanoparticles form longer chains, while other nanoparticles have begun to etch. After 400 s, the nanoparticles are coalescing and dissolving simultaneously as seen in frames at 400, 450 and 540 s, but some structures remain even after 540 s of exposure as shown in the final frame of Fig. 3. Here, we note the similarities in morphology between 181 s of exposure at 200 $e^-/Å^2/s$ in Fig. 2 with that of the 400 s exposure at 100 $e^-/Å^2/s$ in Fig. 3. These represent a similar cumulative dose (~40000 $e^-/Å^2$), and this may suggest that the damage mechanism is accumulated electron dose dependent rather than dose rate dependent. For more details, see video 2 in SI.

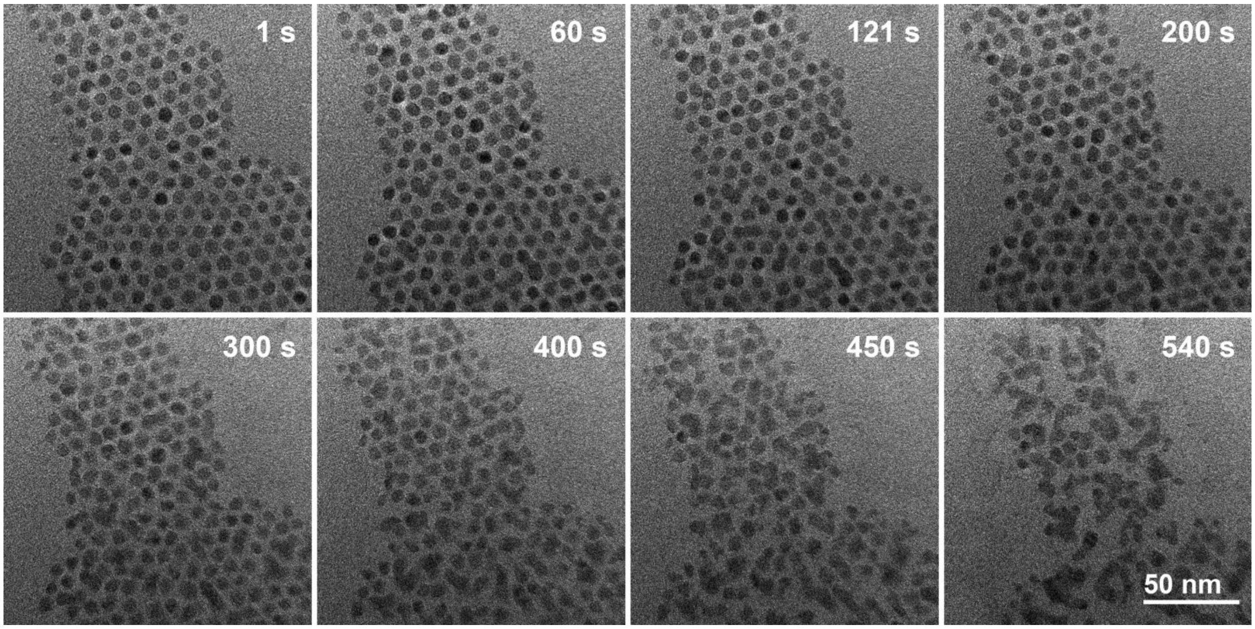

Figure 3. Bright field TEM images of dissolution of PbTe nanoparticles in toluene with an electron dose rate of 100 e$^-$/Å^2/s (medium dose rate) during LCTEM. As in Fig. 2, the total elapsed time of exposure to beam is shown on each frame, and the initial ensemble of nanoparticles has the same distribution as seen with *ex situ* TEM.

Lastly, we performed the same experiment using the lowest electron dose rate exposure of 50 e$^-$/Å^2/s in a nearby unirradiated region as seen in Fig. 4 (taken from Video 3, SI). Here, unlike with the higher doses, we observed no significant structural changes even after a continuous 5-minute exposure to the electron beam, which is vitally important for subsequent experiments in which the TEM shall be used to interrogate, but not alter, the behavior of nanoparticles in organic solvents, whether it be to image oriented attachment, superstructure assembly, shell-growth, etc.

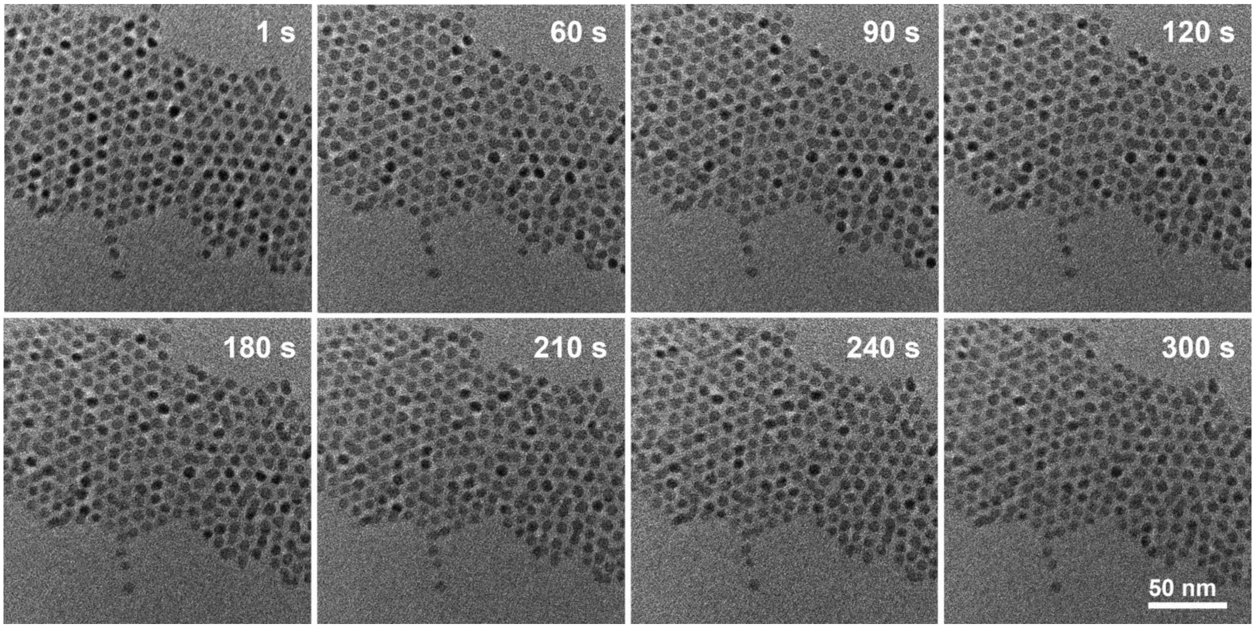

Figure 4. Bright field TEM images of PbTe nanoparticles in toluene as seen under electron dose rate of

50 $e^-/Å^2/s$ (low dose rate) during LCTEM. As in Figs. 2 & 3, the total elapsed time of exposure to beam is shown on each frame, and the initial ensemble of nanoparticles have the same distribution as seen with *ex situ* TEM. For more details, see video 3 in SI.

We can thus radically alter the behavior of the nanoparticles in liquid under the beam depending on the electron dose rate, ranging from no dissolution after 300 s exposure at 50 $e^-/Å^2/s$ to complete dissolution of the entire assembly after 420 s at 200 $e^-/Å^2/s$. During high-dose irradiation, we also note the nucleation of smaller nanoparticles in regions surrounding the initial nanoparticle assembly, which we suggest to arise from either excess Pb in the solution from the initial PbTe nanoparticle synthesis or PbTe byproducts formed during the dissolution of the PbTe nanoparticles.

In contrast to numerous studies that show dissolution of nanoparticles due to oxidative etching from the radiolytic byproducts of electron-irradiated water, [17, 18, 33, 37] the radiolysis of organic solvents, such as those used here, introduces less reactive radiolytic species. For instance, Wu *et al.* recently demonstrated the dissolution of 20 nm sized Pt nanoparticle in aqueous medium using electron dose rates of 30 $e^-/Å^2/sec$,[17] but the direct comparison of electron dose rates in water versus organic solvents is difficult since more radicals are formed in aqueous media. Less radicals are formed in organic solvents partially because the energy transfer from an energetic electron beam to toluene molecules is shared by all π-electrons, which decreases probabilities for ionization.[38] Additionally, toluene's ~24 nm Onsager length (the distance available for electrons, radicals, and ions to recombine) allows a larger number of ions and radicals to recombine yielding less overall ions and free radicals than during radiolysis of water and polar solvents, which have smaller Onsager lengths, ~0.7 and ~10 nm, respectively.[39] Therefore, keeping all other conditions the same, it is expected that higher electron dose rates are required for dissolution of the particles in an organic medium than in an aqueous medium; thus, our experimental results showing electron dose rate for dissolution ~100 $e^-/Å^2/sec$ agrees well with the electron dose rate of 30 $e^-/Å^2/sec$ from the Wu et al. case using aqueous medium.[17]

It is also interesting to compare the effect of different orgranic solvents on the dissolution. The radiolysis of toluene mainly yields molecular hydrogen (H_2) and bibenzyl radicals ($(C_6H_5CH_2)_2$),[30, 39] where bibenzyl radicals are assumed to have negligible effect on dissolution. However, molecular hydrogen may act as a reducing agent, and to investigate its role in dissolution, we changed the solvent from toluene to a (1:1 by volume) mixture of dichlorobenzene (DCB) and pentadecene, where yield of molecular hydrogen during radiolysis should be decreased compared to toluene.[30] As with toluene, the nanoparticles were dispersed in the solvent and loaded into the *in situ* cell in air following the procedures outlined in the Experimental section. Three different electron dose rates (low, medium and high) were again used to study the nanoparticles behavior during TEM imaging. For brevity, we do not show all three cases here, but an example of imaging the nanoparticles at high dose rate is presented in Fig. 5 where the dynamics of PbTe nanoparticles in dichlorobenzene and pentadecane mirror those in toluene and exhibit electron-dose-rate-dependent dissolution after a threshold dose rate above 50 $e^-/Å^2/sec$ despite the lower H_2 yield in the radiolysis of DCB and pentadecene compared to toluene. We understand these results to suggest that the role of hydrogen in dissolution is negligible.

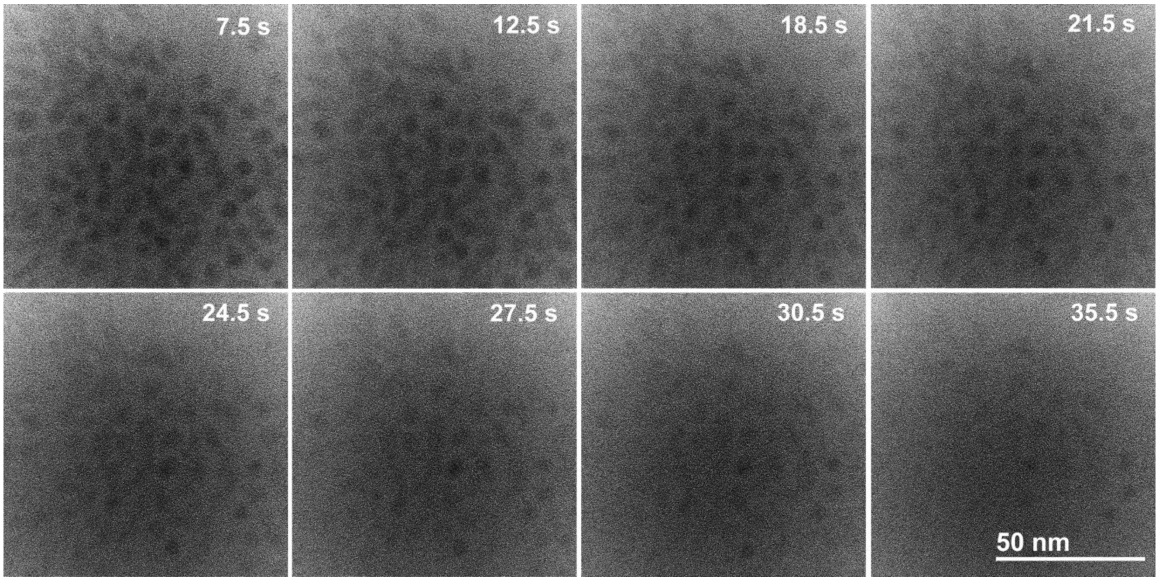

Figure 5: Selected frames of the *in situ* TEM videos of PbTe nanoparticles dispersed in a 1:1 by volume mixture of dichlorobenzene and pentadecene. The elapsed time is shown on each frame.

We propose two mechanisms for the dissolution of PbTe nanoparticles under electron irradiation in organic solvents. With the first mechanism, radiolysis of adsorbed water molecules on membrane surfaces creates oxidizing species and etching of particles takes place similar to previously reported dissolution studies in water. In ambient conditions, it is known that layers of water molecules rapidly adsorb on silicon oxide surfaces, similar to our silicon nitride surfaces, which leads to non-negligible amounts of water content.[40] Based on several adsorbed monolayers of water molecules, or about ~ 1nm thick layer of water, and the ~ 50-100 nm separation, we estimate the water content to be on the order of 1-3%. This water then radiolyzes under exposure to the electron beam causing the resultant cascade of chemically active species, esp. hydroxide ions, which are initiated above an electron dose rate threshold of ~50 $e^-/Å^2/s$. Above this threshold, the concentration of OH^- radicals is high enough to alter nanoparticles, ultimately leading to complete dissolution for higher electron dose rates. With the second mechanism, exposure to ambient conditions during the loading process allows oxygen to be absorbed into the solvent(s). This oxygen in turn reacts with the benzyl radical by-products of the radiolysis of toluene, and the resultant peroxy radicals are reduced to benzylaldehyde and hydroxyl ions, ultimately forming water, which itself is the subject to radiolysis. As with the first mechanism, the prolonged radiolysis of water produces the OH^- radicals, oxidizing the PbTe nanoparticles and initiating the etching of particles.

We can then test this hypothesis by intentionally increasing the water content in the toluene in which the nanoparticles are dispersed. The results of this study are shown in Fig. S2. Here, we are imaging PbTe nanocrystals in water saturated (~0.027 M) toluene at dose rate of ~50 $e^-/Å^2/s$, similar to our 'low dose' conditions in Fig. 4. In this high-water regime, the time, or dose, to observe dissolution of the nanoparticles has clearly decreased. We attribute this behaviour to the increase in water content, which then increases the total number of water molecules available to generate chemically active OH^- radicals under electron irradiation. We note that these results compare favourably with those found by Peng *et al.*[41] In this work, LCTEM was performed with PbSe, as opposed to PbTe, nanoparticles exposed to air and oxygen, as opposed to organic solvents. They observe similar morphological changes during electron beam irradiation, which is attributed to ligand removal and slow oxidation of different crystal facets.

To further characterize PbTe nanoparticle in toluene during TEM imaging, dissolution rates of individual isolated nanoparticles were measured. For these studies, we move to an area with few nanoparticles (individual nanoparticles, not large collections of closed-packed nanoparticles as seen in Fig 2-4) without exposing the nanoparticles by deflecting a high dose electron beam with an electrostatic shutter. At t = 0 s, we expose the nanoparticles to the electron beam and see an immediate response via nanoparticle dissolution. The diameters of the nanoparticles were then measured manually every 5 frames of the video until a given nanoparticle could no longer be identified within a frame (typically at diameters < 1-2 nm). The mean diameter of 14 isolated nanoparticles (exposed to a 'high' electron dose rate, > 200 $e^-/Å^2/s$, where the beam was further condensed after experiments in Fig. 2) is presented over a ~2.5 s time span in Figure 6, where the decreasing diameters have a linear dependence on time (-2.7 nm/s) and almost all isolated nanoparticles dissolve within 3 s of exposure to the electron beam at this higher dose rate exposure. Here, each point represents the mean diameter of 14 nanoparticles at that time, and the error bars are the standard deviation. Within this and other data, the dissolution rate varies somewhat from nanoparticle to nanoparticle, and we note that isolated nanoparticles dissolve faster than those in close proximity to other nanoparticles. Video used for Fig. 6 is given in SI (Video S4).

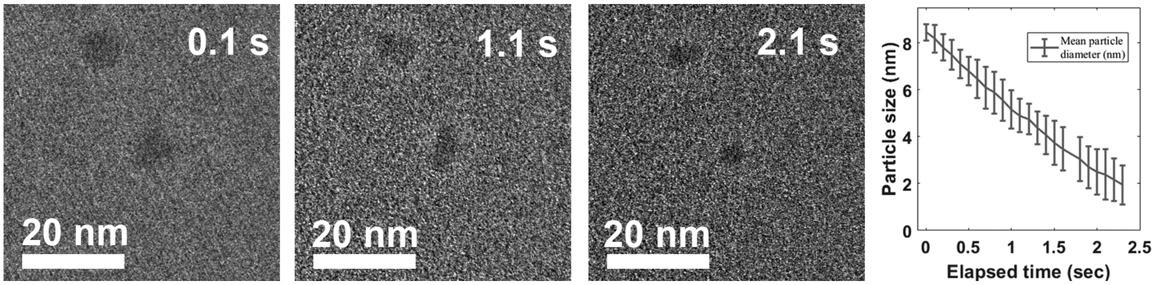

Figure 6: Measuring dissolution of isolated nanoparticles. Elapsed time is shown in left three panels for selected isolated nanoparticles. Right plot shows mean particle diameter (nm) vs elapsed time (s) for 14 isolated nanoparticles, where t = 0 s is defined by the beam shutter.

Having identified a dissolution rate that depends on local nanoparticle concentration as seen by other researchers,[42] i.e. isolated nanoparticles dissolve quicker than close-packed nanoparticles, we similarly posit two reasons for this observation. First, due to the lower concentration of dissolved species near the isolated nanoparticles, the diffusion of dissolved species from the nanoparticle surfaces into the surrounding solvent is higher for isolated nanoparticles than for clusters of more closely packed nanoparticles. Second, the available oxidative etching species per nanoparticle is larger for isolated nanoparticles than for high local nanoparticle concentrations and depletion of etching species slows the dissolution of nanoparticle clusters. Thus, kinetics that depend on local nanoparticle concentration are qualitatively similar to that seen by Jiang *et al* with palladium nanoparticles,[42] but they differ quantitatively in that we do not observe a distinctly non-linear dissolution behavior in nanoparticles with < 5nm radius. Instead, the nanoparticles' roughly linear dissolution rate continues down past the point that we can properly identify individual nanoparticle edges.

4. CONCLUSIONS

In this report, we present electron-dose-rate dependent dissolution of PbTe nanoparticles suspended in organic solvents during LCTEM imaging. For time scales pertinent to LCTEM studies (5-10 min), the particles are completely dissolved for electron dose rates greater than 100 $e^-/Å^2/sec$ while dissolution can be avoided with electron dose rates less than 50 $e^-/Å^2/s$ for nanoparticles loaded in ambient with nominally anhydrous toluene. With toluene that has been intentionally saturated with water, we observe a decrease in the threshold dose rate required for dissolution. Dissolution results from the oxidative etching of nanoparticles by radiolytic by-products produced from the interaction of the electron beam and the nanoparticles' local environment. In addition, this controlled experiment provides direct evidence that LCTEM can be used to study phenomena such as oriented attachment, assembly, and growth of nanoparticles in organic solvents without altering the kinetics when using electron dose rates below a given threshold. Thus, LCTEM with low dose rate conditions can reliably be used to study the formation of PbTe NRs. Even though dissolution may be deleterious, direct imaging of this phenomenon can be used to understand the effect of the radiolysis of liquids near the nanoparticles. This report shows that small amounts of adsorbed ambient water and/or oxygen can lead to degradation of the nanoparticles in otherwise pure organic solvents during LCTEM, and should be helpful in the design of similar experiments and in the study of more elaborate lead-chalcogen nanostructures.

ASSOCIATED CONTENT

Supporting Information

In situ TEM videos for different electron dose rates and solvents are included in the electronic Supporting Information (SI) which is available at DOI.

AUTHOR INFORMATION

Corresponding Author

Todd Brintlinger

Notes

The authors declare no competing financial interest.

ACKNOWLEDGEMENTS

The authors acknowledge funding from the Office of Naval Research. This research was performed while N.B. and D.L.W. held National Research Council Research Associate Awards at the U.S. Naval Research Laboratory.

References

1. D. H. Cui, J. Xu, T. Zhu, G. Paradee, S. Ashok and M. Gerhold, *Appl Phys Lett*, 2006, **88**.
2. D. F. Qi, M. Fischbein, M. Drndic and S. Selmic, *Appl Phys Lett*, 2005, **86**.
3. T. C. Harman, P. J. Taylor, M. P. Walsh and B. E. LaForge, *Science*, 2002, **297**, 2229-2232.
4. J. E. Murphy, M. C. Beard, A. G. Norman, S. P. Ahrenkiel, J. C. Johnson, P. Yu, O. I. Mićić, R. J. Ellingson and A. J. Nozik, *J Am Chem Soc*, 2006, **128**, 3241-3247.
5. P. D. Cunningham, J. E. Boercker, D. Placencia and J. G. Tischler, *Acs Nano*, 2014, **8**, 581-590.
6. L. A. Padilha, J. T. Stewart, R. L. Sandberg, W. K. Bae, W. K. Koh, J. M. Pietryga and V. I. Klimov, *Nano Lett*, 2013, **13**, 1092-1099.
7. J. E. Boercker, E. E. Foos, D. Placencia and J. G. Tischler, *J Am Chem Soc*, 2013, **135**, 15071-15076.
8. W. K. Koh, C. B. Murray, A. C. Bartnik and F. W. Wise, *Abstr Pap Am Chem S*, 2010, **240**.
9. D. Placencia, J. E. Boercker, E. E. Foos and J. G. Tischler, *J Phys Chem Lett*, 2015, **6**, 3360-3364.
10. N. Ziqubu, K. Ramasamy, P. V. S. R. Rajasekhar, N. Revaprasadu and P. O'Brien, *Chem Mater*, 2010, **22**, 3817-3819.
11. X. Pang, Y. He, J. Jung and Z. Lin, *Science*, 2016, **353**, 1268-1272.
12. *Liquid Cell Electron Microscopy*, Cambridge University Press, Cambridge, 2016.
13. A. V. Ievlev, S. Jesse, T. J. Cochell, R. R. Unocic, V. A. Protopopescu and S. V. Kalinin, *Acs Nano*, 2015, **9**, 11784-11791.
14. F. M. Ross, *Science*, 2015, **350**.
15. H.-G. Liao, L. Cui, S. Whitelam and H. Zheng, *Science*, 2012, **336**, 1011-1014.
16. T. J. Woehl, C. Park, J. E. Evans, I. Arslan, W. D. Ristenpart and N. D. Browning, *Nano Lett*, 2014, **14**, 373-378.
17. J. Wu, W. Gao, H. Yang and J.-M. Zuo, *Acs Nano*, 2017, **11**, 1696-1703.
18. X. Ye, M. R. Jones, L. B. Frechette, Q. Chen, A. S. Powers, P. Ercius, G. Dunn, G. M. Rotskoff, S. C. Nguyen, V. P. Adiga, A. Zettl, E. Rabani, P. L. Geissler and A. P. Alivisatos, *Science*, 2016, **354**, 874-877.
19. K. L. Jungjohann, S. Bliznakov, P. W. Sutter, E. A. Stach and E. A. Sutter, *Nano Lett*, 2013, **13**, 2964-2970.
20. W. C. Lee, B. H. Kim, S. Choi, S. Takeuchi and J. Park, *The Journal of Physical Chemistry Letters*, 2017, **8**, 647-654.
21. E. Sutter, P. Sutter, A. V. Tkachenko, R. Krahne, J. de Graaf, M. Arciniegas and L. Manna, *Nature Communications*, 2016, **7**, 11213.
22. S. F. Tan, S. W. Chee, G. Lin and U. Mirsaidov, *Accounts of Chemical Research*, 2017, **50**, 1303-1312.
23. Y. Zhang, D. Keller, M. D. Rossell and R. Erni, *Chem Mater*, 2017, **29**, 10518-10525.
24. P. Abellan, T. J. Woehl, L. R. Parent, N. D. Browning, J. E. Evans and I. Arslan, *Chemical Communications*, 2014, **50**, 4873-4880.
25. L. R. Parent, E. Bakalis, M. Proetto, Y. Li, C. Park, F. Zerbetto and N. C. Gianneschi, *Accounts of Chemical Research*, 2017, DOI: 10.1021/acs.accounts.7b00331.
26. R. G. Weiner, D. P. Chen, R. R. Unocic and S. E. Skrabalak, *Small*, 2016, **12**, 2701-2706.
27. T. J. Woehl, J. E. Evans, I. Arslan, W. D. Ristenpart and N. D. Browning, *Acs Nano*, 2012, **6**, 8599-8610.
28. J. H. Park, N. M. Schneider, J. M. Grogan, M. C. Reuter, H. H. Bau, S. Kodambaka and F. M. Ross, *Nano Lett*, 2015, **15**, 5314-5320.
29. S. Le Caër, *Water*, 2011, **3**.
30. L. H. Gale, B. E. Gordon, G. Steinberg and C. D. Wagner, *The Journal of Physical Chemistry*, 1962, **66**, 1538-1539.

31. J. Park, H. Zheng, W. C. Lee, P. L. Geissler, E. Rabani and A. P. Alivisatos, *Acs Nano*, 2012, **6**, 2078-2085.
32. J. E. Evans, K. L. Jungjohann, N. D. Browning and I. Arslan, *Nano Lett*, 2011, **11**, 2809-2813.
33. Y. Jiang, G. Zhu, F. Lin, H. Zhang, C. Jin, J. Yuan, D. Yang and Z. Zhang, *Nano Lett*, 2014, **14**, 3761-3765.
34. J. Kirchnerová and G. C. B. Cave, *Canadian Journal of Chemistry*, 1976, **54**, 3909-3916.
35. T. Mokari, M. Zhang and P. Yang, *J Am Chem Soc*, 2007, **129**, 9864-9865.
36. I. Moreels, B. Fritzinger, J. C. Martins and Z. Hens, *J Am Chem Soc*, 2008, **130**, 15081-15086.
37. J. R. Eskelsen, J. Xu, M. Y. Chiu, J.-W. Moon, B. O. Wilkins, D. E. Graham, B. Gu and E. M. Pierce, *Environmental Science & Technology*, 2017, DOI: 10.1021/acs.est.7b04343.
38. M. l. S. Maurizot, *Radiation chemistry: from basics to applications in material and life sciences*, EDP Sciences, 2008.
39. P. Abellan, L. R. Parent, N. Al Hasan, C. Park, I. Arslan, A. M. Karim, J. E. Evans and N. D. Browning, *Langmuir*, 2016, **32**, 1468-1477.
40. D. B. Asay and S. H. Kim, *The Journal of Physical Chemistry B*, 2005, **109**, 16760-16763.
41. X. Peng, A. Abelson, Y. Wang, C. Qian, J. Shangguan, Q. Zhang, L. Yu, Z.-W. Yin, W. Zheng, K. C. Bustillo, X. Guo, H.-G. Liao, S.-G. Sun, M. Law and H. Zheng, *Chem Mater*, 2019, **31**, 190-199.
42. Y. Jiang, G. Zhu, G. Dong, F. Lin, H. Zhang, J. Yuan, Z. Zhang and C. Jin, *Micron*, 2017, **97**, 22-28.